Factors Affecting Lift-Drag Ratios at Mach Numbers from 5 to 20

T. P. GOEBEL,* J. J. MARTIN,† AND J. A. BOYD‡
North American Aviation Inc., Los Angeles, Calif.

Yawed-cone working charts and an engineering method are presented and used to calculate lift-drag ratios of flat-top conical wing-body arrangements at Mach numbers from 5 to 20. Viscous interaction effects are considered, but bluntness effects are neglected. Correlations of wind-tunnel data in the range $0.1 \leq [M_\infty^3/(Re_{L\infty})^{1/2}] \leq 1.1$ show that boundary layer displacement corrections to surface pressure and skin friction are required to calculate lift-drag ratios by this method whenever $[M_\infty^3/(Re_{L\infty})^{1/2}]$ is greater than 0.2. M_∞ is the freestream Mach number and $Re_{L\infty}$ is the freestream Reynolds number based on body length. Double- and single-type shock patterns, transition from one pattern to the other, and the variation of inner-shock position with angle of attack are described. Lift-drag ratios are calculated at selected flight design points for flat-top, conical body arrangements with triangular and hyperbolic wing planforms. The hyperbolic wing arrangement offers a potential L/D benefit at Mach 5 but not at Mach 10 or above.

Nomenclature

R, ω, ϕ = spherical coordinates with origin at the vertex of the bow shock
U, V, W = velocity components in the R, ω, ϕ directions made nondimensional by division by V_m
V_m = maximum speed obtainable by expansion into a vacuum, fps
p = static pressure, psf
ρ = fluid density, slugs/ft^3
h = static enthalpy, Btu/lb
μ = dynamic viscosity, lb-sec/ft^2
γ = ratio of specific heats
α = angle of attack, deg
δ_c or τ = semi-cone angle, deg
θ_{W_c} = cone shock wave angle, deg
L_B = body length, ft
λ = wing semi-apex angle, deg
L_W = wing length, ft
M = Mach number
Re = Reynolds number
RF = roughness factor
TF = transition factor
C_p = pressure coefficient
a' = coefficient presented in Appendix C of Ref. 3 for effect of wall temperature on viscous interaction
$\bar{x}$ = hypersonic viscous interaction parameter $[M_\infty^3 C^{1/2}/(Re_{L\infty})^{1/2}]$
C = constant in the secant temperature viscosity relation $(\mu_w T_\infty/\mu_\infty T_w)$
Ap, Bp, Dp = coefficients in second-order expansion in α for cone surface pressure
A_W = coefficient in first-order expansion in α for circumferential velocity near the surface of a cone
$\bar{p}, \bar{a}^2, \bar{u}$ = pressure, speed of sound squared, and radial velocity component for unyawed cone; tabulated in Ref. 9
$x, z, (\eta/p), (\xi/\rho), d$ = coefficients in first-order expansion tabulated in Ref. 10
$u_0, u_2, w_2, p_0, p_2, \rho_0, \rho_2$ = coefficients in second-order expansion tabulated in Ref. 11
γ_E = effective ratio of specific heats which gives the correct density ratio across a real gas shock when used in ideal gas equations
b = parameter that specifies position on starting line
Δ^* = bow shock stand-off distance
C_F = mean skin-friction coefficient
$\bar{C}_F$ = mean skin-friction coefficient neglecting boundary layer displacement correction
V = body volume, ft^3
S_W = planform area, ft^2
q_T = stagnation point convective heating rate, Btu/ft^2-sec

Presented at the IAS National Summer Meeting, Los Angeles, Calif., June 19–22, 1962; revision received January 7, 1963.
* Senior Technical Specialist.
† Aerodynamic Engineer.
‡ Senior Engineer.

Introduction

AT air vehicle speeds appreciably below orbital velocity, aerodynamic lift-to-drag-ratios are of primary interest for range considerations. As vehicle speeds approach orbital velocity, the aerodynamic lift-to-drag ratios are no longer of interest for range considerations but remain of interest for maneuvering and trajectory control. At and above orbital velocity, thermal difficulties are encountered and have focused attention on blunt configurations with relatively high wave drag and relatively low lift-to-drag ratios.

Allen discussed the role of lift-drag ratios in hypersonic vehicle design in his 1957 Wright Brothers Lecture.[26] Brown and McLean[27] discussed maximum lift-drag ratios at low supersonic Mach numbers. Moore and Cheng[28] discussed some of the representative features of hypersonic flow around slender lifting configurations. Geiger[29] reported lift and drag measurements for a series of hypersonic glider configurations. Fowell[30] presented equations and trial computations for analysis of lifting re-entry configurations by the method of characteristics. Now in this paper, approximate techniques are described which are useful in the design of relatively slender configurations for high lift-to-drag ratios at small angles of attack and at velocities appreciably below orbital velocity but still high enough so that the linearized supersonic small disturbance theory cannot be applied.

Correlation of Wind-Tunnel Data

This section summarizes calculations and correlations that were made during the development of a digital computer program to calculate lift-drag ratios of conical wing-body combinations such as illustrated on Fig. 1. A pointed half-cone of circular cross section is mounted below a flat triangular wing with sharp leading edge. Possible shock wave pat-

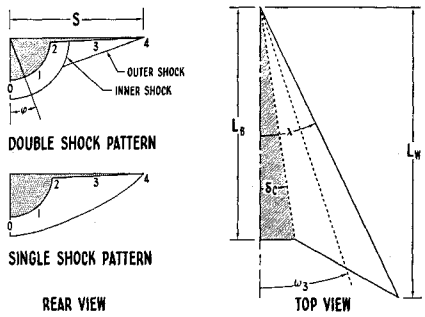

Fig. 1 Geometry of conical wing body configurations

terns that may occur underneath a configuration of this type are sketched on the left-hand side of Fig. 1. Savin[1] assumed the attached single shock pattern and restricted the angle of attack and Mach number to small ranges where this assumption is expected to be valid. One objective of the present study is to develop a method for calculating lift-drag ratios of conical configurations over a broad Mach number, Reynolds number, and angle of attack spectrum. Both the single and the double shock patterns are considered here. Undersurface pressures are required at the points 0 to 4 as shown on Fig. 1. The present method includes the reference temperature, or reference enthalpy, technique,[2] and a boundary layer displacement correction[3] for estimating mean skin friction.

A simplifying assumption is made that the wing boundary layer does not affect the type of shock pattern below the wing-body combination. This assumption is checked by comparison with one set of measured surface pressure data at $[M_\infty{}^3/(Re_{L\infty})^{1/2}] = 0.344$ and is considered to be a reasonable assumption for viscous hypersonic interaction parameter values of $[M_\infty{}^3/(Re_{L\infty})^{1/2}] \leq 1.1$ with wall temperatures approaching the adiabatic wall temperature, and $(a'\bar{x}) \leq 0.7$ for arbitrary wall temperatures. M_∞ is the freestream Mach number, $Re_{L\infty}$ is the Reynolds number based on freestream density and kinematic viscosity and on body length or wing root chord, a' is the function of wall temperature plotted on Fig. 16 of Ref. 3, and $\bar{x}$ is the most frequently used form for the viscous interaction parameter and is defined by Eq. (A20) in Appendix A.

The approximate procedure that has been used to obtain the surface pressures below a conical wing-body combination uses the inner shock position shown on Fig. 2. Since the boundary layer effect on the inner shock position is neglected, the inner shock position at zero angle of attack can be obtained from cone flow tables and graphs, such as presented in Refs. 9, 23, and 24, or can be read from Fig. 3. It is assumed that the inner shock reaches the leading edge and merges with the leading edge shock at the angle of attack for wing shock detachment. This angle of attack for wing shock detachment can be calculated from oblique shock results[23] or read from Fig. 4. The initial slope of the inner shock position vs angle of attack can be calculated by a variety of approximate methods and a parabola fitted to a point slope and point. A few trial computations, however, indicate that this refinement is unnecessary and that the curve of inner shock position vs angle of attack can be determined rather well from only the two points shown on Fig. 2.

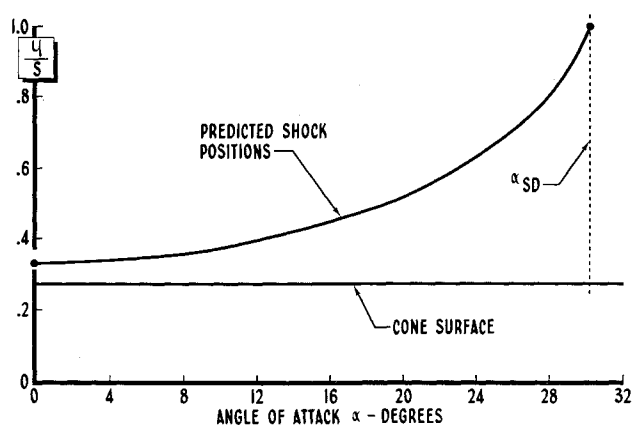

Fig. 2 Inner shock position vs angle of attack

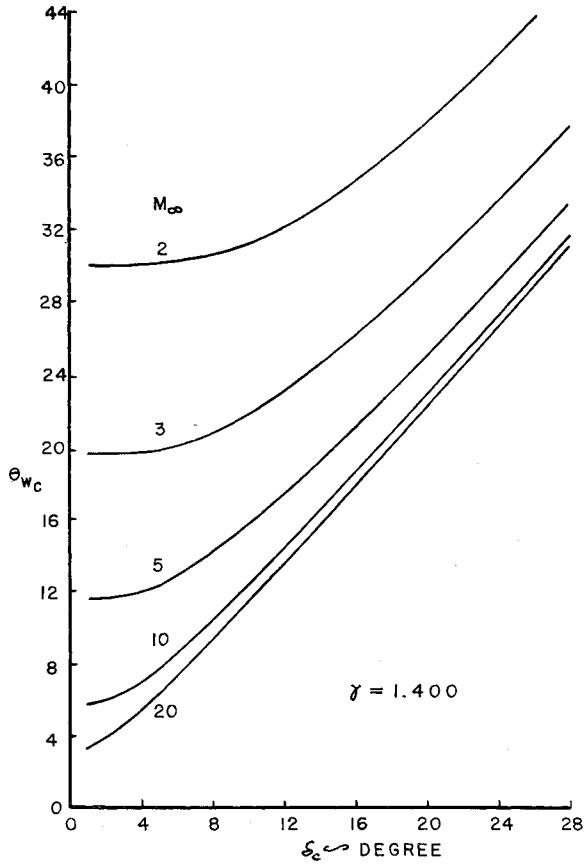

Fig. 3 Cone flow shock wave angles

A typical undersurface pressure distribution is shown on Fig. 5 for the double shock pattern. The second-order, yawed cone pressures are used within 45° meridian angle of the fuselage bottom centerline. These pressures are obtained by inserting the Ap, Bp, and Dp coefficients from Figs. 6–8 into Eq. (B9) of Appendix B. The zero yaw cone pressure p can be obtained from Ref. 9, 23, or 24 or read from Fig. 9. Two-dimensional oblique shock pressures are used on the wing outboard of the inner shock. Between the inner shock and the wing-fuselage juncture, the pressure is assumed to be the average of the fuselage bottom centerline pressure and the two-dimensional oblique shock pressure. At angles of attack above that where the inner shock merges with the outer shock, the undersurface wing pressures still are

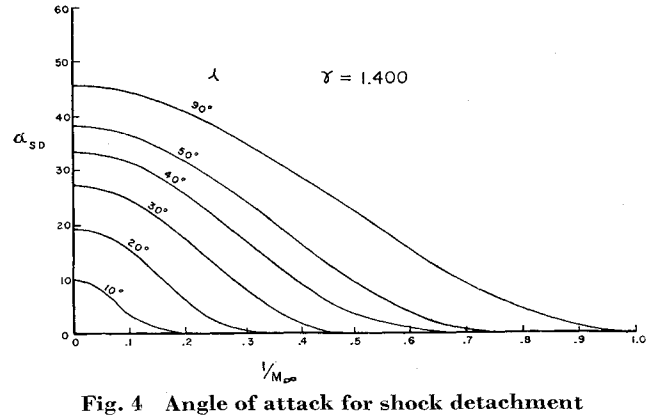

Fig. 4 Angle of attack for shock detachment

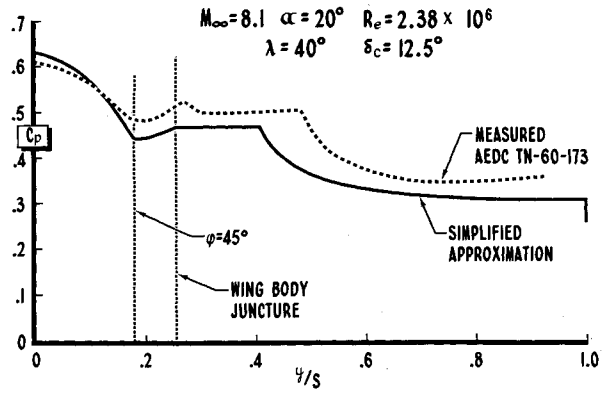

Fig. 5 Double shock-type pressure distribution

assumed to be the average of the fuselage bottom centerline pressure and the two-dimensional oblique shock pressure. This is the approximate procedure that has been used to obtain the undersurface pressures required in the lift-drag ratio calculation reported herein. Other procedures can be, and often are, used with the equations outlined in Appendix A.

The five cases listed on Table 1 have been studied to check the usefulness of the present method. Surface pressure data[6] and force data[7] are available for the first model, W_4B_1.§ Lift-to-drag ratios have been observed by W. O. Armstrong and C. L. Ladson of the NASA Langley Research Center for models A, B, and C. The surface pressure data can be used to correlate the inner shock positions, and the force data can be used to correlate normal force, axial force, lift, drag, and lift-drag ratios. These correlations indicate that, at wind-tunnel conditions, the boundary layer did have appreciable effect on the surface pressures, but no consistent outward displacement of the inner shock due to boundary layer was apparent. These correlations indicate further that, when $[M_\infty{}^3/(Re_{L\infty})^{1/2}] \geq 0.2$, a boundary layer displacement correction of skin friction is required to compute the measured lift-drag ratios. Some caution is required in interpreting the results on Table 1 because systematic errors are not reflected always in lift-drag ratios. This happens, for example, when both the normal force and axial force are calculated low and the lift-drag ratio is calculated as measured.

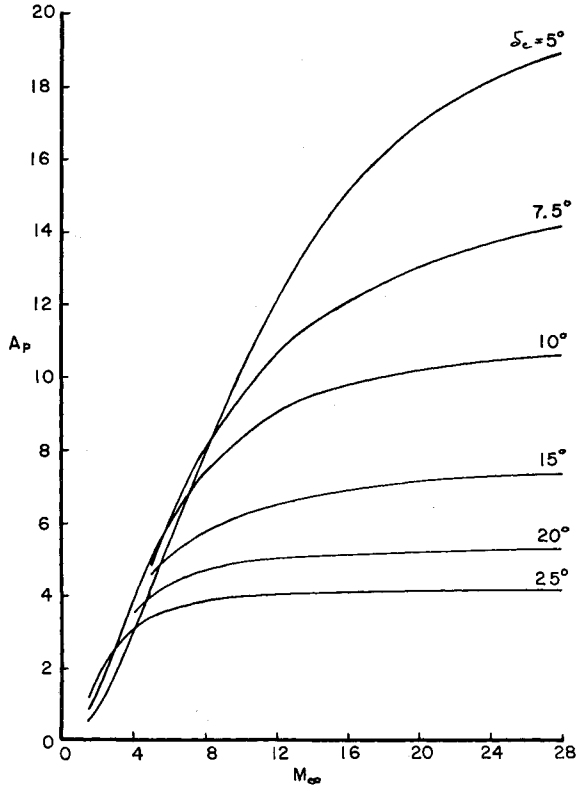

Fig. 6 A_p coefficient

§ These data are discussed in Ref. 25.

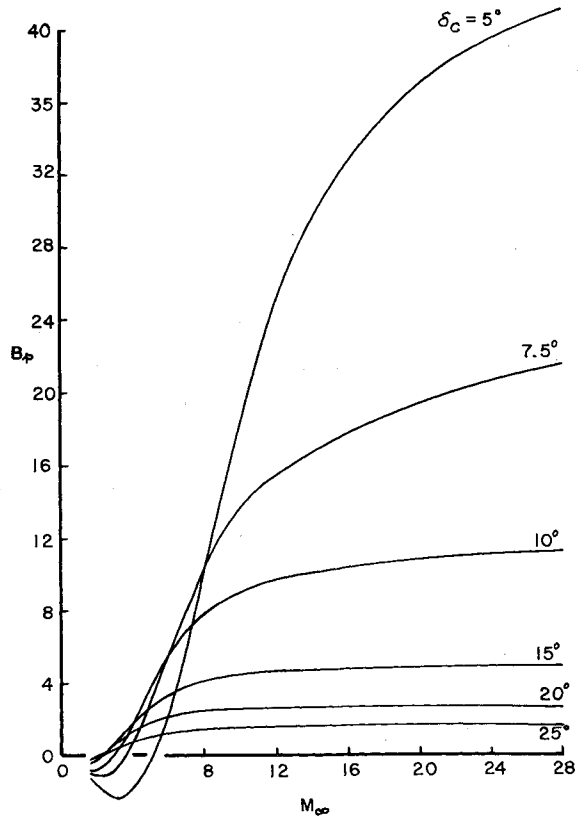

Fig. 7 B_p coefficient

C. H. McLellan of the NASA Langley Research Center has suggested a correlation of maximum lift-drag ratio vs a parameter $(V^{2/3}/S_W)$ for a fixed Mach number and for a restricted range of Reynolds numbers, where V is the body volume and S_W is the wing planform area. Figure 10 indicates the usefulness of a $(V^{2/3}/S_W)$ correlation at Mach number 6.8 and shows, at the same time, the degree of success achieved by the present scheme for calculating maximum lift-drag ratios of conical wing-body arrangements A, B, and C of Table 1. An interesting sidelight on this correlation is provided by the trend of maximum L/D with increasing (λ/θ_{Wc}) when the cone angle is held constant, where λ is

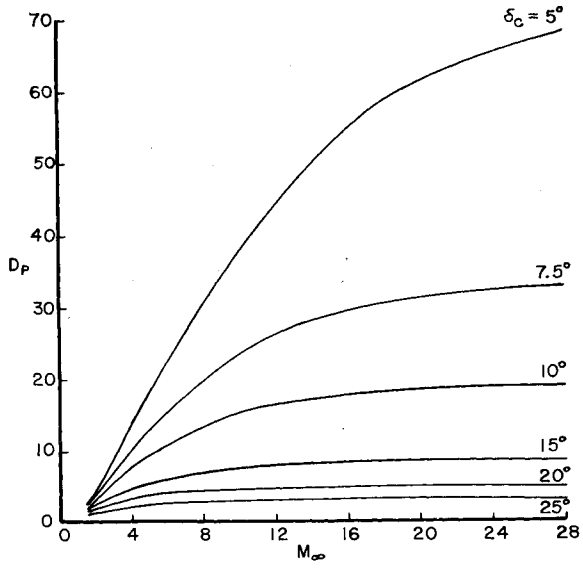

Fig. 8 D_p coefficient

Table 1 Summary of wind tunnel conditions

Model	δ_c, deg	λ, deg	M_∞	$Re_{L\infty}$	$\frac{M_\infty^3}{(Re_{L\infty})^{1/2}}$	$\frac{L_W}{L_B}$	$\frac{V^{2/3}}{S_W}$	Maximum measured, L/D	Maximum calculated, L/D^a
W_4B_1	12.5	25.0	8.10	2.38×10^6	0.344	1.000	0.187	3.02	$2.85T$ $3.23L$
A	5.0	18.0	6.86	1.30×10^6	0.282	1.000	0.101	5.14	$4.85T$ $5.29L$
B	7.5	18.8	6.86	1.30×10^6	0.282	1.000	0.153	3.80	$4.04T$ $4.46L$
C	5.0	12.5	6.86	3.00×10^6	0.186	1.254	0.124	5.26	$5.36T$ $6.30L$
C	5.0	12.5	9.60	7.00×10^5	1.054	1.254	0.124	3.68	$3.40L$

[a] T = turbulent skin friction and L = laminar skin friction.

the wing semi-apex angle and θ_{W_c} is the cone shock wave angle. As λ increases, the $(V^{2/3}/S_W)$ parameter decreases. According to the correlation of Fig. 10, maximum L/D should increase with increasing (λ/θ_{W_c}). This trend is, in fact, observed when the upper-surface streamwise wedge angle is held constant as λ is varied. Isolated exceptions to this trend have been found by Armstrong and Ladson when the upper-surface streamwise wedge angle increases with increasing λ.

Selection of Flight Conditions

The velocity region of interest is restricted so that at least a third of the air vehicle weight is supported by aerodynamic lift. The Mach number range from 5 to 20 and a semi-cone angle of 5° have been selected to cover a hypersonic similarity parameter range from $M_\infty\delta_c = 0.44$ to $M_\infty\delta_c = 1.75$ with constant usable volume inside the body. As indicated in Fig. 11, the altitude range at each Mach number has been selected to bracket the altitudes that could be reached in an equilibrium glide descent from orbit, or in constant altitude

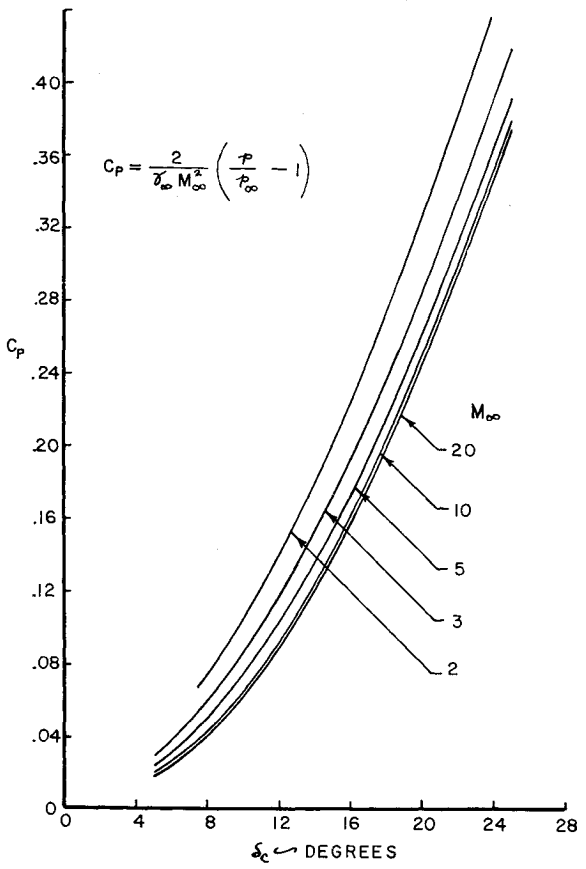

Fig. 9 Unyawed cone pressure coefficient

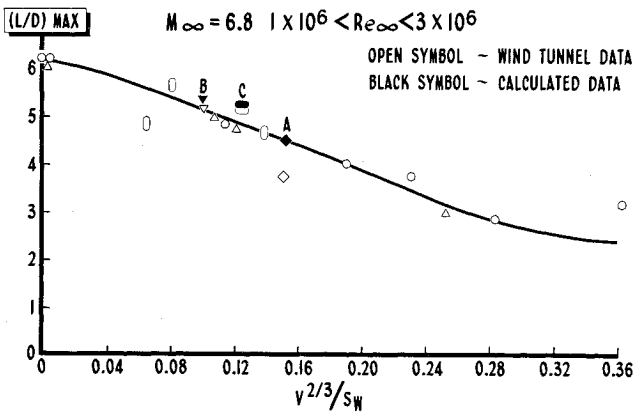

Fig. 10 Untrimmed $(L/D)_{max}$ correlation

powered flight, for a design lift coefficient of 0.1 and wing loadings from 5 to 100 psf. The wing semi-apex angles have been selected at 1.1 to 1.3 times the zero angle of attack cone shock wave angle at each combination of Mach number and cone angle. The delta wing geometries are summarized on Table 2. Except near the wing-body nose, a temperature of 1800°F has been selected as a reasonable working temperature for a radiation-cooled outer wall. The length of the wing and the body is taken as 100 ft. The wing is a 2° sharp leading edge, full blunt wedge. The bottom of the wing is flat and lies in the fuselage reference plane. The fuselage is a 5° pointed circular half-cone with its axis of symmetry in the plane of the flat undersurface of the wing.

Altitude velocity conditions are shown in Fig. 11 as analysis points. Relevant parameters are summarized on Tables 3 and 4. The ARDC 1959 standard atmosphere model has been used in these computations. Transition factors TF used in the computation of lift-drag ratios are listed on Table 4. A roughness factor RF of 1 is used for all analysis points. Equations for calculating L/D values are outlined in Appendix A.

Table 2 Delta wing geometry

M	λ/θ_{W_c}	λ, deg	S_W, ft^2
5	1.1	13.50	2400
	1.2	14.74	2636
	1.3	16.00	2868
10	1.1	8.52	1500
	1.2	9.30	1639
	1.3	10.06	1770
15	1.1	7.70	1352
	1.2	8.41	1480
	1.3	9.11	1604
20	1.1	6.88	1208
	1.2	7.52	1320
	1.3	8.13	1430

Table 3 Summary of flight conditions ($\delta_c = 5°$; $\delta_W = 2°$; $L = 100$ ft; $T_W \geq 1800°$F)

W	Altitude, 1000 ft	$Re_{L\infty}$	h_{AW} Btu/lb	$\frac{h_W}{h_{AW}}$	$\frac{M_\infty{}^3}{(Re_{L\infty})^{1/2}}$	$\bar{x}_\infty$	$a'\bar{x}$	$\frac{C_F}{\bar{C}_F}$
5	80	1.42×10^8	511	1.000	0.011	0.008	0.006	1.009
	120	1.98×10^7	590	0.968	0.027	0.022	0.013	1.020
	160	3.65×10^6	665	0.863	0.066	0.051	0.026	1.039
10	120	3.96×10^7	2037	0.283	0.159	0.123	0.026	1.039
	160	7.30×10^6	2296	0.250	0.370	0.284	0.051	1.077
	200	1.88×10^6	2026	0.284	0.729	0.565	0.119	1.179
15	140	2.45×10^7	4767	0.120	0.680	0.531	0.074	1.111
	180	5.44×10^6	4901	0.117	1.444	1.130	0.158	1.237
	220	1.87×10^6	3946	0.146	2.465	1.881	0.282	1.421
20	180	7.46×10^6	8621	0.067	2.930	2.292	0.280	1.418
	210	2.92×10^6	7360	0.078	4.681	3.603	0.450	1.666
	240	2.18×10^6	6105	0.094	5.420	4.086	0.531	1.782

Table 4 Summary of flight conditions ($\delta_c = 5°$; $\delta_W = 2°$; $L = 100$ ft; $T_W \geq 1800°$F)

M	Altitude, 1000 ft	$Re_{L\infty}$	TF (estimated)	Dynamic pressure, psf	q_T for 1-ft nose radius, Btu/ft²-sec	T_{equil} 1 ft aft of leading edge, °F
5	80	1.42×10^8	1.000	1018	23	1050
	120	1.98×10^7	1.000	172	11	800
	160	3.65×10^6	0.965	37	6	610
10	120	3.96×10^7	1.000	689	86	1550
	160	7.30×10^6	0.990	149	46	1150
	200	1.88×10^6	0.840	33	20	700
15	140	2.45×10^7	1.000	700	213	1780
	180	5.44×10^6	0.985	162	106	1240
	220	1.87×10^6	0.840	32	39	770
20	180	7.46×10^6	0.990	288	252	1470
	210	2.92×10^6	0.910	88	122	1080
	240	2.18×10^6	0.870	23	53	740

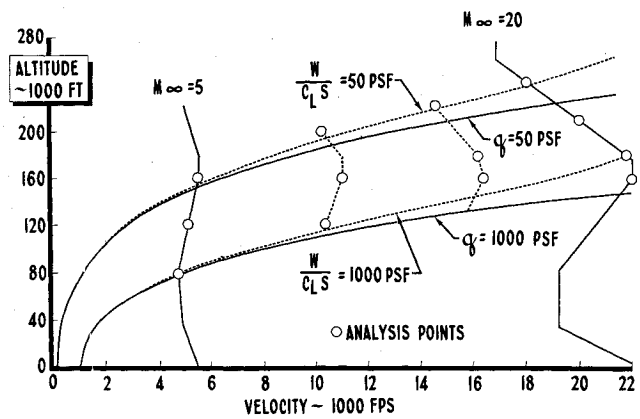

Fig. 11 Altitude velocity region of interest

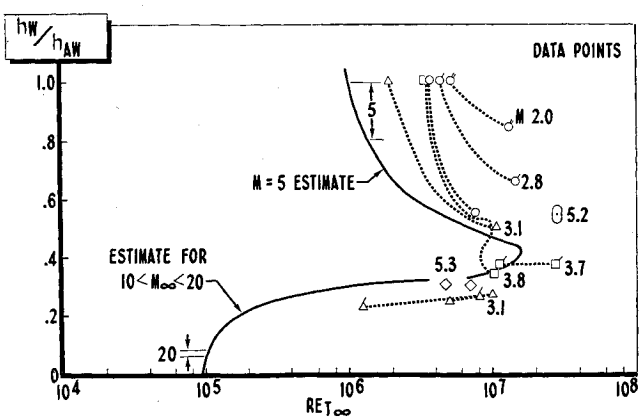

Fig. 12 Estimated transition Reynolds number

Boundary Layer Transition

Recently published observations of boundary layer transition are summarized on Table 5 and Fig. 12. Experimental evidence can be found for moderate boundary layer stabilization by cooling at low supersonic Mach numbers and at Reynolds numbers between 10^6 and 10^7. Transition Reynolds number estimates are shown on Fig. 12 for the conical flat-top configurations considered in this study. The approximate range of enthalpy ratios resulting from the assumed wall temperature of 1800°F are indicated on Fig. 12 for Mach numbers 5 and 20. Very few transition observations have been reported at the small enthalpy ratios of interest as Mach numbers approach 20.

Table 5 Transition data shown on Fig. 12

Symbol	M	Body type	Facility	Reference
◇	1.97	5° cone	wind tunnel	32
◇	2.81	5° cone	wind tunnel	32
○	3.84	5° cone	wind tunnel	32
△	3.12	5° cone-cylinder	wind tunnel	33
△	3.1	5° cone	free-flight ballistic model	34
□	3.8	6.25° cone	wind tunnel	35
□	3.6 to 3.9	10° cone-cylinder	free-flight rocket model	35
⬯	5.15	7.5° cone	free-flight rocket model	36
◇	5.3	ogive-cylinder	free-flight ballistic model	37

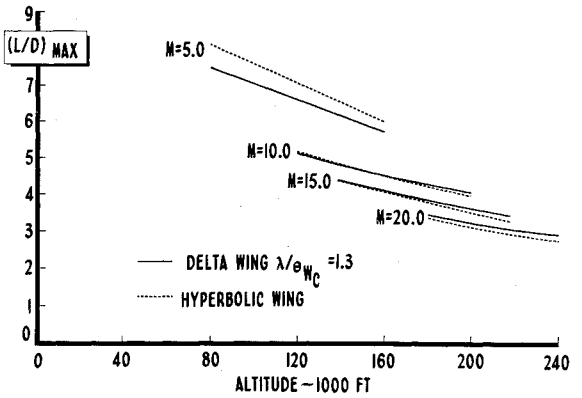

Fig. 13 Untrimmed maximum L/D vs altitude

Lift-to-Drag Ratios at Flight Conditions

The variations of maximum design L/D with design altitude for delta wing combinations of $(\lambda/\theta_{W_c}) = 1.3$ are shown as solid curves on Fig. 13. Maximum L/D decreases with increasing design altitude and design Mach number. As indicated on Table 2, the wing area decreases and the body volume remains constant as the Mach number increases at a constant value of (λ/θ_{W_c}). Corresponding values of angle of attack, lift coefficient, and drag coefficient at maximum L/D are shown on Fig. 14.

Maximum L/D values were calculated for the triangular wing arrangement with $(\lambda/\theta_{W_c}) = 1.1$ and 1.3. At Mach 5 and 160,000-ft altitude, L/D maximum increased by 4.0% as (λ/θ_{W_c}) increased from 1.1 to 1.3. At Mach 20 and 160,000-ft altitude, L/D maximum increased by 4.4% as (λ/θ_{W_c}) increased from 1.1 to 1.3. The present method gives increasing maximum L/D with increasing (λ/θ_{W_c}). Of the class of configurations shown on Fig. 1, and with volume constraints removed, the maximum L/D is achieved with a thin wing alone.

One possible arrangement of a conical body and a hyperbolic wing is sketched on Fig. 15. In laying out a configuration of this type, it is important to adjust the wing geometry, which is set by the body shock, for the displacement effect of the boundary layer on the body. Detailed fuselage contouring requires some care because vortex shedding from the sides of the fuselage can cause troublesome complications. Potential maximum L/D values have been computed by a simplified procedure and are shown as dashed lines on Fig. 13. A gain in maximum L/D is indicated at Mach 5 by appropriate arrangements of hyperbolic wings and underslung conical bodies.

Requirements for Including Bluntness Effects

So far, no adjustments for bluntness effects have been made to the estimated flow fields or to lift-to-drag ratios. One approximate method that sometimes has been used to estimate pressures on blunted slender bodies is to add tangent cone pressures to hemisphere-cylinder, blunt-nose, carryover pressures. Test data[22] show that this approximate method will not work at hypersonic speeds for a 5° cone because it does not predict the overexpansion. Starting with zero cone angle, that is, with a hemisphere cylinder, one can visualize what happens as the cone angle is increased. Within a low density entropy layer, an increase in cone angle produces almost no increase in pressure. The cone angle does not have to be increased very much before a region of overexpansion is apparent immediately downstream of the hemisphere nose. Farther downstream, as the high density shock layer approaches the surface, an increase in pressure is observed.

One of the more satisfying analyses of bluntness effects to be published within recent years is Ref. 21 by Cheng.

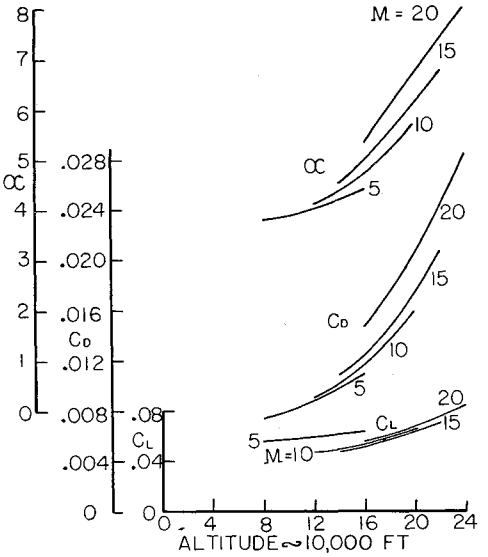

Fig. 14 C_L, C_D, and α at maximum L/D

He considers that, far downstream of a blunt nose, an appropriate flow model is composed of three layers: 1) an outer, high-density shock layer; 2) an inter, low-density, high-temperature entropy layer; and 3) an inner, low-velocity boundary layer. A region of overexpansion is found when a 5° cone is blunted with a hemisphere. This is indicated by Cheng's theoretical analysis and verified by measurements.[22] Figure 6a of Cheng's paper[21] shows the effects of nose drag coefficient and of ratio of specific heats on the position of the outer edge of the entropy layer.

The region of overexpansion extends for 40 to 80 nose radii downstream of the nose for the basic 5° cone used in the present study. Unless a nose can be designed of radius appreciably less than 1 ft, this region of overexpansion will include a significant portion of a 100-ft wing length.

The lifting effectiveness of the wing is reduced if the entire wing is within a low dynamic pressure entropy layer. Similarly, if the entire wing is within the high dynamic pressure shock layer, the lifting effectiveness of the wing is increased. When the wing surface includes both the high-density shock layer and the low-density entropy layer, it is not immediately obvious whether a small amount of blunting will cause an increase or a decrease in lift-drag ratio. A small amount of blunting may cause the inner shock, which is shown on Fig. 1, to disappear entirely.

A flow structure must be assumed before a flow field analysis can be carried out. One approach is to adapt the three-layer model[21] to a blunted configuration of the type shown on Fig. 1. A second approach is to estimate a boundary layer displacement thickness and to use the method of Appendix C, or one of the alternate methods mentioned in Appendix C, to start a three-dimensional, method-of-characteristics computation of the downstream inviscid flow. In either case, the inner shock shown on Fig. 1 may reappear in the flow far

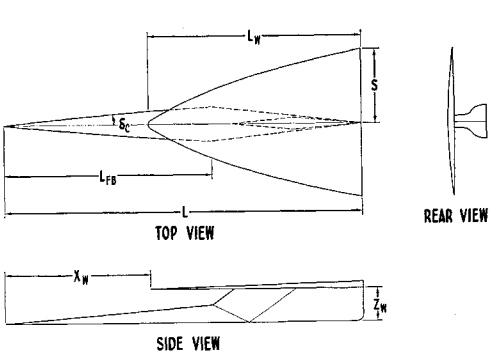

Fig. 15 Geometry of hyperbolic-wing configuration

downstream of the nose. Fowell[30] has mentioned some of the difficulties that are encountered in a three-dimensional, method-of-characteristics computation.

Limitations of Local Boundary Layer Similarity

Whenever the longitudinal or transverse pressure gradients change appreciably within several boundary layer thicknesses, results that have been obtained by assuming similar velocity profiles within the boundary layer are always subject to question. Within such areas, for example, as near the intersection of the inner shock and the wing surface and immediately downstream of a blunt nose, the local boundary layer characteristics are expected to differ from those that would be calculated by assuming local boundary layer similarity. The mean skin friction on a slender configuration, however, probably still is given to sufficient accuracy by a similarity analysis, such as used by Cheng.[21]

Suggestions for Further Study

Among the physical phenomena that affect lift-to-drag ratios at Mach numbers from 5 to 20 and that require more careful evaluation are 1) boundary layer transition, 2) boundary layer displacement of the inviscid flow, and 3) wing-body pressure and vortex field interactions.

Appendix A: Lift-Drag Ratios

Simplified equations are presented for the lift-drag ratios of flat-top, conical wing-body configurations. The surface pressure coefficients are assumed given at the five positions numbered underneath the configuration on Fig. 1. The equations are restricted by taking the wing length L_W equal to the body length L_B. The equations have been adapted from a Fortran program that is essentially an extension of a method outlined by Savin[1] and allows a more detailed pressure distribution to be used. Savin's method[1] allowed pressure information to be used at the fuselage bottom centerline, at the wing-body juncture, and at the wing leading edge. The present equations provide a better interpolation capability by allowing pressure information to be used at one additional location on the body and one additional location on the wing.

Customary laminar and turbulent flat-plate skin-friction equations are used to calculate the mean skin friction. Effects of Mach number and average wall temperature are approximated by use of a Reynolds number based on an intermediate reference temperature T^* as suggested in Ref. 2. An appropriate reference chord is used to establish the average skin friction of a triangular wing and is based on calculations presented in Appendix D of Ref. 3. A correction for the effect of boundary layer displacement on the mean skin friction is included and has been adapted from Appendix C of Ref. 3. The effect of average wall temperature on boundary layer displacement thickness is approximated by an a' coefficient presented by Bertram[3] and based on the strong interaction analysis of Li and Nagamatsu[4] for hypersonic viscous flow on a noninsulated flat plate. This correction, which is applicable to a laminar boundary layer on a delta wing, is applied to the skin friction of the entire configuration regardless of the condition of the boundary layer. A control Reynolds number is based on freestream velocity and kinematic viscosity and on either body length or wing root chord. A transition factor TF is used to locate the mean skin friction between the laminar and turbulent levels. An additional roughness factor RF is used to increase the skin friction of turbulent boundary layers due to surface roughness. At an angle of attack near zero, the pressures around a wing-body combination are averaged to give a representative pressure level p_δ. A mean skin friction is calculated at this pressure level for the corresponding T_δ and M_δ. As the configuration is pitched to angle of attack, the increase in skin friction on one surface is assumed to be compensated by a decrease in skin friction on the other surface. The axial force due to skin friction is, therefore, independent of angle of attack, and the method is restricted to angles of attack less than about 10°.

The effect of base pressure on axial force coefficient is neglected. This is equivalent to setting the base pressure equal to the freestream static pressure.

Equations (A1–A5) give the normal and axial force coefficients based on wing planform area and freestream dynamic pressure. Equations (A6–A22) give the skin friction coefficient based on wetted area and freestream dynamic pressure. Equation (A23) gives the lift-drag ratio:

$$C_{N_W} = \left[\frac{\tan\omega_3 - \tan\delta_c}{\tan\lambda}\right]\left[C_{p_3} + \frac{1}{3}(C_{p_2} - C_{p_3})\right] + \left[1 - \frac{\tan\omega_3}{\tan\lambda}\right]\left[C_{p_4} + \frac{1}{3}(C_{p_3} - C_{p_4})\right] + (\Delta C_{N_W})_E \quad \text{(A1)}$$

$$C_{N_B} = \frac{\tan\delta_c}{\tan\lambda}\left\{\left[\frac{C_{p_0} + C_{p_1}}{2}\right][\sin\phi_1] + \left[\frac{C_{p_1} + C_{p_2}}{2}\right] \times [1 - \sin\phi_1] + \left[\frac{C_{p_0} - C_{p_1}}{4}\right]\left[\frac{2\phi_1^2 \sin\phi_1}{\pi^2 - \phi_1^2}\right] + \left[\frac{C_{p_1} - C_{p_2}}{4}\right] \times \left[\frac{2[(\pi/2) - \phi_1]^2 \cos^2\phi_1}{\pi^2 - [(\pi/2) - \phi_1]^2}\right]\right\} \quad \text{(A2)}$$

$$C_{A_B} = \frac{\tan^2\delta_c}{\tan\lambda}\left\{\left[\frac{C_{p_0} + C_{p_1}}{2}\right][\phi_1] + \left[\frac{C_{p_1} + C_{p_2}}{2}\right] \times \left[\frac{\pi}{2} - \phi_1\right]\right\} + (C_{F_\infty})_B\left(\frac{\pi}{2}\frac{\tan\delta_c}{\tan\lambda}\sec\delta_c\right) \quad \text{(A3)}$$

$$C_{A_W} = -(\Delta C_{N_W})_E \tan\delta_w + (C_{F_\infty})_W\left(2 - \frac{\tan\delta_c}{\tan\lambda}\right) \quad \text{(A4)}$$

$$(\Delta C_{N_W})_E = -\frac{2}{\gamma_\infty M_\infty^2} \times \left\{\left[1 - \frac{\gamma_\infty - 1}{2} M_\infty(\alpha - \delta_W)\right]^{2\gamma_\infty/(\gamma_\infty - 1)} - 1\right\} \quad \text{(A5)}$$

$$M_\delta = (M_\delta/M_\infty)M_\infty \quad \text{(A6)}$$

$$T_{A_W}/T_\delta = 1 + r[(\gamma - 1)/2]M_\delta^2 \quad \text{(A7)}$$

$r = 0.85$ (laminar)
$r = 0.89$ (turbulent)

$$T^*/T_\infty = \{0.28 + [0.22 + 0.50(T_W/T_{A_W})] \times (T_{A_W}/T_\delta)\}(T_\delta/T_\infty) \quad \text{(A8)}$$

$$\frac{\mu^*}{\mu} = \left[\frac{1 + (S/T_\infty)}{(T^*/T_\infty) + (S/T_\infty)}\right]\left(\frac{T^*}{T_\infty}\right)^{3/2}$$

$S = 198°\text{R}$ (A9)

$$\rho^*/\rho_\infty = (p_\delta/p_\infty)/(T^*/T_\infty) \quad \text{(A10)}$$

$$Re^* = Re_{L_\infty}(\rho^*/\rho_\infty)(M_\delta/M_\infty)(T_\delta/T_\infty)^{1/2}(\mu_\infty/\mu^*) \quad \text{(A11)}$$

$$C_F^* = 1.328/(0.5625\ Re^*)^{1/2} \quad \text{laminar wing} \quad \text{(A12)}$$

$$C_F^* = 0.455/[\log_{10}(0.5905 Re^*)]^{2.584} \quad \text{turbulent wing} \quad \text{(A13)}$$

$$C_F^* = 1.533/(Re^*)^{1/2} \quad \text{laminar cone} \quad \text{(A14)}$$

$$C_F^* = 0.469/[\log_{10} Re^*]^{2.584} \quad \text{turbulent cone} \quad \text{(A15)}$$

$$\bar{C}_{F_\infty} = C_F^*(\rho^*/\rho_\infty)(M_\delta/M_\infty)^2(T_\delta/T_\infty) \quad \text{(A16)}$$

$$\bar{C}_{F_\infty} = (\bar{C}_{F_\infty})_{\text{laminar}} + TF[RF(\bar{C}_{F_\infty})_{\text{turbulent}} - (\bar{C}_{F_\infty})_{\text{laminar}}] \quad \text{(A17)}$$

$$T_W/T_\infty = (T_W/T_{AW})(T_{AW}/T_\delta)(T_\delta/T_\infty) \quad \text{(A18)}$$

$$C = \left[\frac{1 + (S/T_\infty)}{(T_w/T_\infty) + (S/T_\infty)}\right]\left(\frac{T_W}{T_\infty}\right)^{1/2} \quad \text{(A19)}$$

$$\bar{x} = M_\infty{}^3 C^{1/2}/(Re_{L\infty})^{1/2} \quad \text{(A20)}$$

$$C_{F\infty} = \bar{C}_{F\infty}[1 + \tfrac{3}{2}(a'\bar{x}) - \tfrac{1}{10}(a'\bar{x})^3] \qquad (a'\bar{x}) \leq 1 \quad \text{(A21)}$$

$$C_{F\infty} = \bar{C}_{F\infty}\left(\tfrac{12}{5}\right)(a'\bar{x})^{1/2} \qquad (a'\bar{x}) > 1 \quad \text{(A22)}$$

$$\frac{L}{D} = \frac{(C_{NW} + C_{NB})\cos\alpha - (C_{AW} + C_{AB})\sin\alpha}{(C_{AW} + C_{AB})\cos\alpha + (C_{NW} + C_{NB})\sin\alpha} \quad \text{(A23)}$$

Appendix B: Cone Flow Coefficients

An analytical expression has been developed by Cheng[5] for the pressure field around yawing cones. The cone surface pressure is, in Cheng's notation,

$$p_{CH} = \bar{p}_{CH} + \left[\frac{\epsilon}{\cos\tau}\left(\frac{\sin^2\tau}{2} - \frac{4}{15}\right) - 2\cos\tau\right]\sigma\sin\omega + \left[\cos 2\tau - \cos^2\omega\left(\cos^2\tau + \frac{1}{4}\right)\right]\sigma^2 \quad \text{(B1)}$$

$$\bar{p}_{CH} = 1 + \frac{\epsilon}{4} + \frac{5}{4}\epsilon\kappa + \epsilon^2\left[\frac{3}{32} + \frac{\tan^2\delta_c}{4}\right] \quad \text{(B2)}$$

$$p_{CH} = p/\rho_\infty U_\infty{}^2 \sin^2\tau \quad \text{(B3)}$$

$$\bar{p}_{CH} = \bar{p}/\rho_\infty U_\infty{}^2 \sin^2\tau \quad \text{(B4)}$$

$$\sigma = \sin\alpha/\sin\tau \quad \text{(B5)}$$

$$\omega = \phi - (\pi/2) \quad \text{(B6)}$$

$$\epsilon = (\gamma - 1)/(\gamma + 1) \quad \text{(B7)}$$

$$\kappa = [(\gamma + 1)/(\gamma - 1)](1/\gamma M_\infty{}^2 \sin^2\tau) \quad \text{(B8)}$$

If Eq. (B1) is transferred into the notation of this paper and if the $\sin\alpha$ is replaced with α, there is obtained

$$p/\bar{p} = 1 + A\alpha\cos\phi + (B + D\cos^2\phi)\alpha^2 \quad \text{(B9)}$$

where the coefficients A_p, B_p, and D_p are given by

$$A_p = \left(\frac{2}{\tan\delta_c} + \frac{4(\gamma - 1)}{15(\gamma + 1)\sin\delta_c\cos\delta_c} - \frac{(\gamma - 1)\tan\delta_c}{(\gamma + 1)}\right)\times\left(\frac{1}{\bar{p}_{CH}}\right) \quad \text{(B10)}$$

$$B_p = \left(\frac{3}{2\tan^2\delta_c} - \frac{9}{8\sin^2\delta_c}\right)\left(\frac{1}{\bar{p}_{CH}}\right) \quad \text{(B11)}$$

$$D_p = \left(\frac{1}{2\tan^2\delta_c} + \frac{1}{8\sin^2\delta_c}\right)\left(\frac{1}{\bar{p}_{CH}}\right) \quad \text{(B12)}$$

$$\bar{p}_{CH} = 1 + \left(\frac{\gamma - 1}{\gamma + 1}\right)\left(\frac{1}{4}\right) + \frac{5}{4\gamma M_\infty{}^2\sin^2\delta_c} + \left(\frac{\gamma - 1}{\gamma + 1}\right)^2\left[\frac{3}{32} + \frac{\tan^2\delta_c}{4}\right] \quad \text{(B13)}$$

Similar expressions can be obtained for the circumferential velocity at the surface of a yawed cone. To the first order in angle of attack, this circumferential velocity is not influenced by the existence of a vortical layer on the cone surface:

$$W = A_W\alpha\sin\phi \quad \text{(B14)}$$

$$A_W = \frac{U_\infty}{V_m}\left\{2\left(\frac{\gamma - 1}{\gamma + 1}\right) + \left(\frac{\gamma - 1}{\gamma + 1}\right)^2\times\left[\frac{23\sec^2\delta_c}{30} - 1\right] + \frac{2}{\gamma M_\infty{}^2\sin^2\delta_c}\right\} \quad \text{(B15)}$$

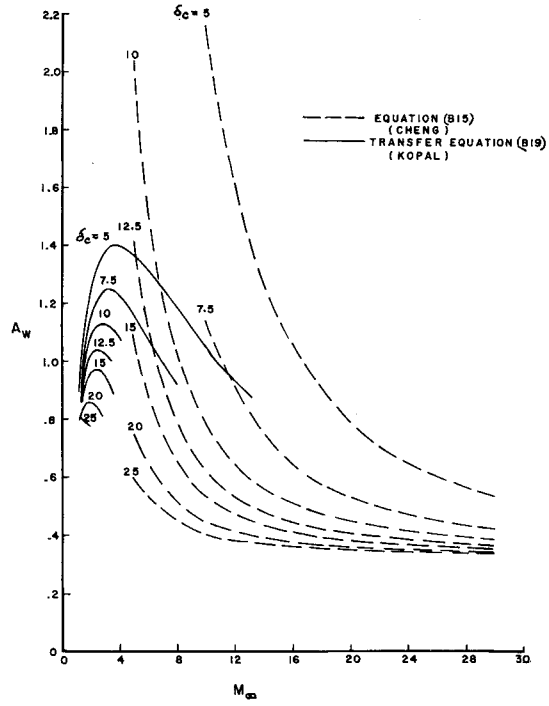

Fig. 16 A_W coefficient

The coefficients Ap, Bp, Dp, and A_W in Eqs. (B9) and (B14) also can be evaluated from data tabulated in Refs. 9–11 and transferred to the body axes system following the instructions of Ref. 12. The parameters on the right-hand side of Eqs. (B16–B19) are tabulated in Refs. 10 and 11 and are expressed in the notation of those reports:

$$Ap = \eta/p \quad \text{(B16)}$$

$$B_p = (p_0/\bar{p}) + (\gamma\bar{u}^2/2\bar{a}^2) + (\eta^3 2\bar{p})\cot\delta_c \quad \text{(B17)}$$

$$D_p = (p_2/\bar{p}) + (\gamma\bar{u}^2/2\bar{a}^2) - (\eta/2\bar{p})\cot\delta_c \quad \text{(B18)}$$

$$A_W = -z - (2x/\sin\delta_c) = \bar{u}(\bar{a}^2 Ap/\gamma\,\bar{u}^2\sin\delta_c) \quad \text{(B19)}$$

The coefficients given by Eqs. (B10–B15) with $\gamma = 1.405$ have been used[38] to aid in the extrapolation of the Stone-Kopal second-order coefficients to higher Mach numbers. The resulting Ap, Bp, Dp, and A_W coefficients are shown on Figs. 6–8 and 16 for $\gamma = 1.405$. Eqs. (B10–B15) provide values of these coefficients at smaller values of γ.

When the Ap, Bp, Dp coefficients shown on Figs. 6–8 were prepared, a smooth fairing was obtained from the Stone-Kopal results[38] into the Cheng hypersonic shock layer results.[39] This was surprising and encouraging, because Cheng's analysis was carried through for small ϵ, that is for $\gamma \to 1.0$, and this fairing was made for $\gamma = 1.405$. Calculated surface pressures were compared[40] with available measured surface pressures, and the coefficients were evaluated using an alternate theoretical approach.[41] Later, a revision to Ref. 5 was published. Ap, Bp, and Dp were recalculated using the revised equation of Ref. 5. Ap and Dp did not change, and Bp was reduced slightly over the ranges $10 \leq M_\infty \leq 30$ and $5° \leq \delta_c \leq 25°$. More recently, a new form of Cheng's analysis has appeared in Ref. 8. Ap, Bp, and Dp have been calculated again using Eq. (2.9) of Ref. 8 and retaining the $\epsilon^2\kappa^2$ terms that previously had been neglected. The $\bar{p}_{CH}$ values for zero-yaw cone pressures given by either the original or revised Ref. 5 agree well with Kopal-tabulated cone pressures over the ranges $10 \leq M_\infty \leq 30$ and $5° \leq \delta_c \leq 25°$. The $\bar{p}_{CH}$ values given by the present interpretation of Eq. (2.9) of Ref. 8 do not agree with Kopal-tabulated cone pressures over these ranges. Recalculated Ap and Dp values are slightly higher than shown on Figs. 6 and 8

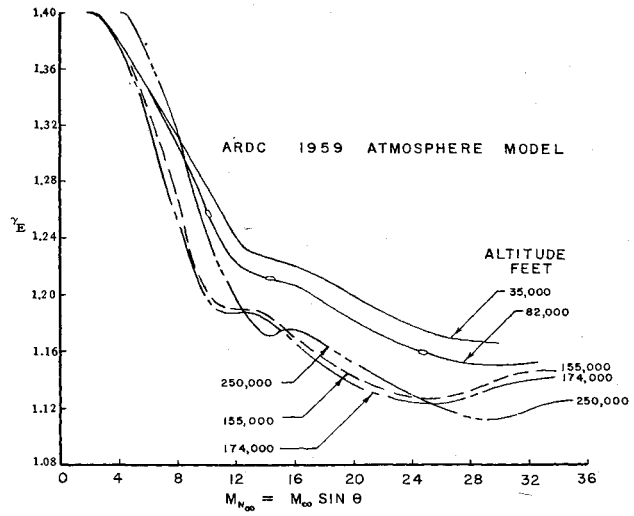

Fig. 17 Effective ratio of specific heats

whereas recalculated Bp values are lower than shown on Fig. 7.

A_W coefficients given by Eqs. (B15) and (B19) are shown on Fig. 16. A similar set of faired A_W coefficients has been presented by Sims.[31]

Appendix C: Blunt Body Starting Data

Among the several ways of starting method-of-characteristics computations at the nose of a three-dimensional blunted body are 1) the Anderson flow structure approximation[19] using an effective gamma concept, 2) the Dorodnitsyn-Belotserkovskii method of integral relations,[13, 14] 3) the Gravalos step-by-step integration method,[15] 4) the Van Dyke inverse procedure,[16] 5) the Ferri Vaglio-Laurin inverse procedure,[17] and 6) the sonic cone approximation.[18] The first method, which is called a flow-structure approximation, has excellent stability of numerical computation, requires a relatively small amount of digital computer time, and includes first-order effects of dissociation of air.

Major simplifying assumptions of the flow structure approximation are as follows:

1) The body is blunted with a segment of a sphere to the starting line or slightly past the body sonic point.

2) Up to the starting line, the bow shock sheet is approximated by a hyperboloid of revolution which has a radius-of-curvature on the body centerline which is equal to the body radius-of-curvature plus the shock stand-off distance.

3) The effective gamma γ_E parameter[19] of Fig. 17 is used to correlate earlier real equilibrium air computations and to obtain fluid-dynamic properties to start the method of characteristics computation along a starting line that extends from the body to the shock and is perpendicular to the body as shown by Fig. 18.

4) The density ratio ϵ is related to the effective gamma γ_E by definition in Eq. (C1).

5) The bow shock stand-off distance is obtained from the density ratio ϵ by a formula developed in Ref. 20 and commonly called the Li and Geiger stand-off distance.

6) The body surface pressure follows a modified Newtonian variation with $\sin^2\theta$ up to the starting line.

Primary Computation

Input data: $M_\infty, \gamma_\infty, p_\infty, M_B, R_B, \gamma_E, b$.

Output data: x, r, p, θ, p_T are obtained by computing

$$\epsilon = \frac{\gamma_E - 1}{\gamma_E + 1} + \frac{2}{M_\infty^2(\gamma_E + 1)} \tag{C1}$$

$$\left(\frac{\Delta^*}{R_S}\right) = -\epsilon\left\{\frac{-1 + [1 - (1-\epsilon)^2]^{1/2}}{(1-\epsilon)^2}\right\} \tag{C2}$$

$$\frac{R_S}{R_B} = \frac{1}{[1 - (\Delta^*/R_S)]} \tag{C3}$$

$$\frac{p_B}{p_{T_B}} = \left[1 + \frac{\gamma_E - 1}{2} M_B^2\right]^{-[\gamma_E/(\gamma_E - 1)]} \tag{C4}$$

$$M_A^2 = \frac{2 + (\gamma_E - 1)M_\infty^2}{2\gamma_E M_\infty^2 - (\gamma_E - 1)} \tag{C5}$$

$$\frac{p_{T_B}}{p_\infty} = \left[1 + \frac{\gamma_E - 1}{2} M_A^2\right]^{\gamma_E/(\gamma_E - 1)} \times \left[\frac{2\gamma_\infty M_\infty^2}{\gamma_E + 1} - \frac{(2\gamma_\infty - \gamma_E - 1)}{\gamma_E + 1}\right] \tag{C6}$$

$$\sin^2\theta_B = \frac{(p_{T_B}/p_\infty)(p_B/p_{T_B}) - 1}{(p_{T_B}/p_\infty) - 1} \tag{C7}$$

$$\frac{r_N}{R_S} = \frac{M_\infty^2 \tan\theta_B - [(M_\infty^2 - 1)^2(1 + \tan^2\theta_B) + M_\infty^2(M_\infty^2 - 1)]^{1/2}}{(1 + \tan^2\theta_B) - M_\infty^2} \tag{C8}$$

$$\Delta/R_B = (r_N/R_S)(R_S/R_B)(1/\cos\theta_B) - 1 \tag{C9}$$

$$x = R_B\{1 - [1 + (\Delta/R_B)b]\sin\theta_B\} \tag{C10}$$

$$r = R_B\{1 + (\Delta/R_B)b\}\cos\theta_B \tag{C11}$$

$$\tan^2\sigma_N = \frac{1}{M_\infty^2 - 1} + \frac{1}{(r_N/R_S)^2} \tag{C12}$$

$$\frac{p_N}{p_\infty} = \frac{2\gamma_\infty}{\gamma_E + 1} M_\infty^2 \sin^2\sigma_N - \frac{2\gamma_\infty - \gamma_E - 1}{\gamma_E + 1} \tag{C13}$$

$$p = p_\infty\left\{(1-b)\left[1 + \left(\frac{p_{T_B}}{p_\infty} - 1\right)\sin^2\theta_B\right] + b\left(\frac{p_N}{p_\infty}\right)\right\} \tag{C14}$$

$$\theta = \theta_B(1-b) + b \times \tan^{-1}\left\{\frac{1}{[(\gamma_E + 1)M_\infty^2/2(M_\infty^2\sin^2\sigma_N - 1)\,1] - \tan\sigma_N}\right\} \tag{C15}$$

$$\tan\beta = (1-b)\tan\theta_B + b\tan\sigma_N \tag{C16}$$

$$\frac{V}{V_\infty} = \frac{(1-\epsilon)^2}{2\epsilon}\cos\beta\left[\left(\frac{\Delta^*}{R_S}b + 1 - \frac{\Delta^*}{R_S}\right)^2 - 1\right] + [\epsilon^2 + (1-\epsilon^2)\cos^2\beta]^{1/2} \tag{C17}$$

$$M^2 = \frac{\gamma_\infty - 1}{\gamma_E - 1} \times \left\{\frac{M_\infty^2(V/V_\infty)^2}{1 + [(\gamma_\infty - 1)/2]M_\infty^2[1 - (V^2/V_\infty^2)]}\right\} \tag{C18}$$

$$p_T = p\{1 + [(\gamma_E - 1)/2]M^2\}^{\gamma_E/(\gamma_E - 1)} \tag{C19}$$

Detailed derivation and discussion of Eqs. (C1–C19) are presented by Anderson.[19] When adjustments are made

to satisfy conservation requirements and boundary conditions more precisely, the results are called a flow-structure refinement to distinguish them from the foregoing flow-structure approximation.

Follow-On Computation

Input data: x, r, p, θ, p_T at $(N + 1)$ points along the starting line and h_T.

Output data: x, r, p, θ, (S/R), h, T, ρ, V, a, μ at $(N + 1)$ points along the starting line.

Step 1: (S/R) is obtained from the given (p_T, h_T) pair using an equilibrium air subroutine.

Step 2: The state properties h, T, and ρ are obtained from the given $(p, S/R)$ pair using this same equilibrium air properties subroutine.

Step 3: The flow properties a, V, and μ are obtained from the given (p, T, h, h_T) values using an auxiliary air properties subroutine.

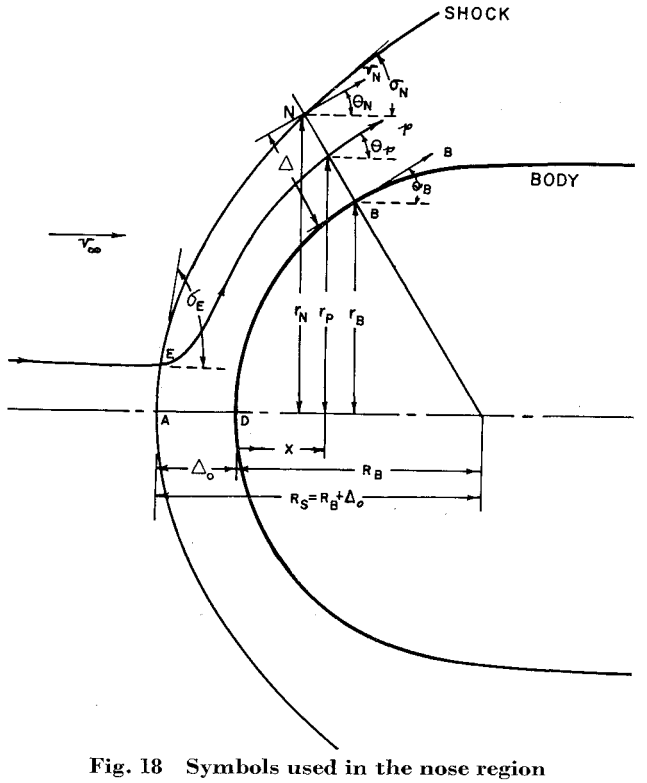

Fig. 18 Symbols used in the nose region

References

[1] Savin, R. C., "Approximate solutions for the flow about flat-top wing-body configurations at high supersonic airspeeds," NACA RM A58F02 (1958).

[2] Eckert, E. R. G., "Engineering relations for friction and heat transfer to surfaces in high velocity flow," J. Aerospace Sci. **22,** 85 (1955).

[3] Bertram, M. H., "Boundary-layer displacement effects in air at Mach numbers of 6.8 and 9.6," NASA TR-R-22 (1959).

[4] Li, T. Y. and Nagamatsu, H. T., "Hypersonic viscous flow on noninsulated flat plate," *Proceedings of the Fourth Midwestern Conference on Fluid Mechanics* (University of Michigan Press, Ann Arbor, Mich., 1956), pp. 273–287.

[5] Cheng, H. K., "Hypersonic shock layer theory of a yawed cone and other three dimensional pointed bodies," Wright Air Dev. Center TN-59-335 (October 1959).

[6] Randall, R. E., Bell, D. R., and Burk, J. L., "Pressure distribution tests of several sharp leading edge wings, bodies, and body-wing combinations at Mach 5 and 8," Arnold Eng. Dev. Center TN-60-173 (September 1960).

[7] Burchfield, C. G., "Force tests of several sharp leading edge wing-body combinations at Mach 8," Arnold Eng. Dev. Center TN-61-46 (May 1961).

[8] Cheng, H. K., "Hypersonic flows past a yawed circular cone and other pointed bodies," J. Fluid Mech. **12,** 169–191 (February 1962).

[9] Kopal, Z., "Tables of supersonic flow around cones," Mass. Inst. Tech. Center of Analysis TR-1 (1947).

[10] Kopal, Z., "Tables of supersonic flow around yawing cones," Mass. Inst. Tech. Center of Analysis TR-3 (1947).

[11] Kopal, Z., "Tables of supersonic flow around cones of large yaw," Mass. Inst. Tech. Center of Analysis TR-5 (1949).

[12] Roberts, R. C. and Riley, J. D., "A guide to the use of the M.I.T. cone tables," J. Aerospace Sci. **21,** 336–342 (1954).

[13] Hayes, W. D. and Probstein, R. F., *Hypersonic Flow Theory* (Academic Press, New York, 1959), pp. 333–370.

[14] Kennet, H., "Some steady and unsteady inviscid hypersonic flows past bluff bodies," Mass. Inst. Tech. D.Sc. Thesis (June 1961).

[15] Gravalos, F. G., Edelfelt, I. H., and Emmons, H. W., "The supersonic flow about a blunt body of revolution for gases at chemical equilibrium," General Electric R-58SD245 (June 1958).

[16] Van Dyke, M. and Gordon, H., "Supersonic flow past a family of blunt axisymmetric bodies," NASA TR-1 (1959).

[17] Vaglio-Laurin, R. and Ferri, A., "Theoretical investigation of the flow field about blunt nosed bodies in supersonic flight," J. Aerospace Sci. **25,** 761–770 (1958).

[18] Van Hise, H., "Analytic study of induced pressure on long bodies of revolution with varying nose bluntness at hypersonic speed," NASA TR-R-78 (1961).

[19] Anderson, A. B. C., "Calculation of flow parameters behind shocks at hypersonic speeds for air in chemical equilibrium," North American Rept. NA-59-1475 (September 1959).

[20] Li, T. Y. and Geiger, R. E., "Stagnation point of a blunt body in hypersonic flow," J. Aerospace Sci. **24,** 25–32 (1957).

[21] Cheng, H. K., "Hypersonic flow with combined leading-edge bluntness and boundary layer displacement effect," AF-1285-A-4, Cornell Aeronaut. Lab. (August 1960).

[22] Burke, A. F. and Curtis, J. T., "Blunt-cone pressure distributions at hypersonic Mach numbers," J. Aerospace Sci. **29,** 237 (1962).

[23] Ames Research Staff, "Equations, tables, and charts for compressible flow," NACA TR-1135 (1953).

[24] Wang, C. J., Goebel, T. P., and Farnell, A. B., "Conical flow tables," North American Rept. NA-55-671 (June 1955).

[25] Scheuing, R. A., "Outer inviscid hypersonic flow with attached shock waves," ARS J. **31,** 486–505 (1961).

[26] Allen, H. J., "Hypersonic flight and the re-entry problem," J. Aerospace Sci. **25,** 217–227 (1958).

[27] Brown, C. E. and McLean, F. E., "The problem of obtaining high lift-drag ratios at supersonic speeds," J. Aerospace Sci. **26,** 298–302 (1959).

[28] Moore, F. K. and Cheng, H. K., "The hypersonic aerodynamics of slender and lifting configurations," Inst. Aerospace Sci. Paper 59-125 (June 1959).

[29] Geiger, R. E., "Experimental lift and drag of a series of glide configurations at Mach numbers 12.6 and 17.5," J. Aerospace Sci. **29,** 410–419 (1962).

[30] Fowell, L. R., "Flow field analysis for lifting re-entry configurations by the method of characteristics," Inst. Aerospace Sci. Paper 61-208-1902 (June 1961).

[31] Sims, J. L., "On conical flow upwash," J. Aerospace Sci. **27,** 952–953 (1960).

[32] Van Driest, E. R. and Boison, J. C., "Experiments on boundary-layer transition at supersonic speeds," J. Aerospace Sci. **24,** 885–899 (1957).

[33] Jack, J. R., Wisniewski, R. J., and Diaconis, N. S., "Effects of extreme cooling on boundary-layer transition," NACA TN-4094 (1957).

[34] Lyons, W. C., Jr. and Sheetz, N. W., Jr., "Transition measurements on cones in free-flight ballistic-range tests," J. Aerospace Sci. **29,** 352 (1962).

[35] Wisniewski, R. J. and Jack, J. R., "Recent studies on the effect of cooling on boundary-layer transition at Mach 4," J. Aerospace Sci. **28,** 250–251 (1961).

[36] Rumsey, C. B. and Lee, D. B., "Measurements of aerodynamic heat transfer and boundary-layer transition on a 15° cone in free-flight at supersonic Mach numbers up to 5.2," NASA TN D-888 (1961).

[37] Carros, R. J., "Effect of Mach number on boundary-layer transition in the presence of pressure rise and surface roughness

on an ogive-cylinder body with cold wall conditions," NACA RM A56B15 (1956).

[38] Goebel, T. P., "Transfer of M. I. T. yawed cone data from wind to body axes," North American Rept., Appendix A, NA-60-952 (July 1960).

[39] Goebel, T. P., "Computation of Ap, Bp, Dp coefficients using Cheng's hypersonic shock layer theory," North American Rept., Appendix D, NA-60-952 (July 1960).

[40] Goebel, T. P., "Correlation of cold-flow, yawed-cone pressure data," North American Rept., Appendix G, NA-60-952 (July 1960).

[41] Goebel, T. P., "Computation of Ap, Bp, Dp coefficients using Newtonian concepts," North American Rept., Appendix E, NA-60-952 (July 1960).

MARCH 1963 AIAA JOURNAL VOL. 1, NO. 3

Nonequilibrium Flow Past a Wedge

R. Capiaux* and M. Washington*
Lockheed Missiles and Space Company, Palo Alto, Calif.

An exact numerical solution is obtained for the chemically reacting flow past a wedge. The freestream is either in equilibrium or out of equilibrium but nonreacting. The attached shock wave is shown to be either concave, convex, or straight, depending on the values of the amount of dissociation in the freestream and a parameter describing the amount of energy contained in the freestream relative to the gas dissociation energy. Numerical examples are presented illustrating these regimes. The flow field is characterized by the presence of an entropy layer and a relaxation layer, both easily identifiable in the presentation of the numerical results.

Introduction

THE equations of motion of a compressible inviscid fluid undergoing chemical reactions and internal relaxation effects have been derived by Wood and Kirkwood.[1] In particular, the authors transform the one-dimensional unsteady flow into a characteristic form and find that the "frozen" speed of sound plays a role analogous to the sound velocity in the case of a nonreactive fluid. Chu[2] arrives at the same conclusion and obtains the characteristic equation for steady two-dimensional and axially symmetric flows.

One of the important differences between a chemically reacting gas flow and a nonreacting or equilibrium flow consists in an entropy production appearing in the energy equation. The entropy production term is a direct result of reactions in the flow field which are thermodynamically irreversible processes.

As Clarke[3] points out, the entropy production is not confined to the interior of boundary layers or shock waves because it is not associated with a transport phenomenon. Its influence therefore can spread over the entire flow field and will not depend explicitly on the gradients of velocity, temperature, and concentration.

In the present paper, a numerical solution is obtained for the chemically reacting, steady, two-dimensional flow past a wedge. This solution is the counterpart of Sedney's solution,[4] which treats the case of the flow of a vibrationally relaxing gas past a wedge. Viscosity, thermal conduction, and diffusion have been neglected purposely to emphasize the forementioned effects. A simple body configuration is selected in order to allow a direct comparison of the results with the simple results associated with a nonreacting fluid. The analysis is applied to a pure diatomic gas, such as oxygen or nitrogen, which obeys the model proposed by Lighthill[5] in its equilibrium dissociated state. The chemistry rate is described appropriately by a somewhat simplified but accurate rate equation introduced by Freeman.[6] The undisturbed fluid is allowed to assume either an equilibrium dissociated state or a nonreacting frozen state. Thus, the degree of dissociation of the freestream determines whether the flow in the wake of the leading shock will undergo a dissociation or recombination process.

The solution previously presented by Vincenti[7] neglects, as a consequence of the linearization assumption, the entropy production term; the flow therefore remains irrotational. In this presentation, the introduction of a streamline oriented coordinate system allows naturally for the accounting of the dissociation and recombination processes and the entropy increase associated with them. The equations of motion then are solved numerically by the method of characteristics.

Two-Dimensional Steady Flow: General Equations

The equations of motion will be derived in this section for a general, diatomic, reacting gas. Specialization to a particular equation of state and rate equation will be introduced in a later section. The geometry of the problem is presented in Fig. 1.

For the case of the two-dimensional flow in Cartesian coordinates, the equations of continuity and of momentum can be written as follows:

$$[\partial(\rho u)/\partial x] + [\partial(\rho v)/\partial y] = 0 \tag{1}$$

$$u(\partial u/\partial x) + v(\partial u/\partial y) = -1/\rho(\partial p/\partial x) \tag{2}$$

$$u(\partial v/\partial x) + v(\partial v/\partial y) = -1/\rho(\partial p/\partial y) \tag{3}$$

Here ρ is the mixture density, p the pressure, and u and v components of the velocity vector V on the x and y axes, respectively.

The energy equation can be written in several equivalent forms. If h is the enthalpy (including the chemical bond energy), t is the time, and D/Dt designates the convective derivative, the following relations hold:

$$\rho(Dh/Dt) - (Dp/Dt) = 0 \tag{4}$$

$$(D/Dt)[h + (V^2/2)] - (1/\rho)(\partial p/\partial t) = 0 \tag{5}$$

For the assumed nonequilibrium situation, the continuity

Presented at the IAS National Summer Meeting, Los Angeles, Calif., June 19–22, 1962; revision received December 17, 1962.

* Member, Fluid Mechanics, Mechanical and Mathematical Sciences Laboratory, Research Laboratories.